

# Low-noise read-out electronics design for a solar soft X-ray spectrometer onboard the MSS-1B satellite\*

Jian-Wu Chen ,<sup>1,†</sup> Yong-Qiang Shi,<sup>1</sup> Fu-Chang Zuo,<sup>1</sup> Zhi-Wu Mei,<sup>1</sup> Wei-Chun Fu,<sup>1</sup> Fang-Qin Gai,<sup>1</sup> Ye Chang,<sup>1</sup> Ying Yang,<sup>1</sup> Shu-Juan Yang,<sup>1</sup> Zhi-Jun Tu,<sup>1</sup> Xu-Li Liu,<sup>1</sup> Jian-Fu Zhang,<sup>1</sup> Ran Zheng,<sup>1</sup> Li Wang,<sup>1</sup> Chun-Hui Zhao,<sup>1</sup> Di Zhang,<sup>2</sup> and Xiao-Ping Zhang <sup>3</sup>

<sup>1</sup>*Beijing Institute of Control Engineering, Beijing 100190, China*

<sup>2</sup>*School of Astronautics, Northwestern Polytechnical University, Xi'an 710072, China*

<sup>3</sup>*State Key Laboratory of Lunar and Planetary Sciences,  
Macau University of Science and Technology, Macau 999078, China*

The main scientific payload of Macau Science Satellite-1B is a solar soft X-ray detection unit. To obtain an accurate solar X-ray spectrum, we have designed low-noise, high-throughput electronics. Solar radiation is detected using a low-leakage silicon drift detector (SDD), which is cooled to  $-30^{\circ}\text{C}$ . The SDD output is processed using two parallel shaping amplifiers with peaking times of 315 ns and 65 ns. The amplifiers are designed using two-pole multiple-feedback active low-pass filters optimized to achieve a Bessel response. The differential output of the shaping amplifier generates a bipolar signal. The phase of the differential stage is tuned to ensure zero crossing corresponding to the peak of the shaping amplifier. A high-speed switch is inserted between the shaping amplifier and the peak-hold capacitor, and the peak value is maintained by turning off the switch. Fast and slow peak-hold circuits share a common ADC via time-division multiplexing. Both peak values are sampled for space-background rejection. Traditional pile-up detection methods cannot distinguish pulses that overlap in a fast channel. In this study, the differential of the “fast shaping” is selected, enabling the distinction of events separated by as little as 65 ns, which is crucial for solar flare detection. The energy resolution is measured to be 138 eV at 5.90 keV. The centroid drift is less than 3.6 eV between  $-5^{\circ}\text{C}$  and  $20^{\circ}\text{C}$ . Compared with other solar X-ray instruments, this study demonstrates improved energy resolution with a lower peaking time, indicating a higher solar flare detection capability.

Keywords: Solar flare, X-ray detector, Energy resolution, Pile-up rejection, Spectroscopy

## I. INTRODUCTION

X-ray astronomy is based on the detection of X-rays from celestial sources [1]. The Macau Science Satellite-1B (MSS-1B) is primarily responsible for monitoring solar activity, particularly solar flares, during Solar Cycle 25 [2]. Its main scientific payload is a solar X-ray detector (SXD) that features a wide energy range and a high count rate. The SXD consists of two soft X-ray detection units (SXDUs) with different aperture areas and two identical hard X-ray detection units (HXDUs). These four detection units are integrated into the instrument. This study focuses on the electronic design of the SXDU. The X-ray sensor (XRS) on the GOES satellite provides continuous solar X-ray flux measurements, and the standard X-ray classification of solar flares is based on these measurements [3, 4]. However, the sensor lacks spectral resolution, which limits the physical investigation of coronal emissions in the X-ray spectrum. The Solar Assembly for X-rays (SAX) on MESSENGER consists of a Si-PIN detector with an aperture area of  $0.03 \text{ mm}^2$ . Its energy resolution is 598 eV at 5.9 keV, which is constrained by Si-PIN noise [5]. The Solar X-ray Spectrometer (SXRS) on the FY-2F mission monitors solar flares above the M1 level with an energy resolution of 185 eV [6]. The HEPP-X onboard the CSES is

designed to monitor the solar radiation from a wide field of view [7]. The X-ray spectrometer on MinXSS detects solar X-rays in the  $0.8 - 12 \text{ keV}$  range with a time cadence of 10 s [8]. The on-orbit energy resolutions for MinXSS-1 and MinXSS-2 at 5.90 keV are 240 eV for a  $4.8 \mu\text{s}$  peaking time and 168 eV for  $1.2 \mu\text{s}$ , respectively [9]. An improved instrument, known as the Dual-Zone Aperture X-ray Solar Spectrometer, employs a newer version of the SDD and a dedicated aperture design [10]. Its cadence time is set to 9 s. Solar observations are limited to flare levels below M3 due to the detector's saturation limit [11]. These CubeSats and instruments are designed using commercial off-the-shelf electronic devices, and one instrument was previously damaged by a single-event latch-up [12]. The Chandrayaan-2 Solar X-ray Monitor measures the  $1-15 \text{ keV}$  spectrum from lunar orbit with an energy resolution of 175 eV at 5.9 keV [13]. Its aperture area is limited to  $0.367 \text{ mm}^2$ , making it feasible for detecting flares up to the M5 class. We enhanced the time cadence to 1 s using a dedicated X-ray signal processing design. The peaking times of the shaping amplifiers were optimized to enhance the energy resolution and achieve higher count rates. In particular, two soft X-ray detector units with different aperture areas were integrated to detect solar irradiation, targeting both the quiet Sun and solar flares up to the X-class level.

The primary working principle of the SXD was presented by Shi et al. [14], whereas this study focuses on a detailed description of the SXDU's electronic design and the results of ground calibration. The remainder of this paper is organized as follows. Section II presents the basic principles, in-

\* This was supported by the National Natural Science Foundation of China (No. 12035020) and National Key Scientific Instrument and Equipment Development Projects of China (No. 42327802).

† Corresponding author, chenjianwumail@163.com

strument composition, and specifications. Sections III–IV describe the design of the X-ray detector module and the analog electronic unit. Section V discusses the scientific data types, while Sect. VI covers spectral performance calibration. Finally, Section VII presents the conclusions.

## II. INSTRUMENT DESIGN

To distinguish the emission lines from those of solar flares, the SXDU is designed with an energy resolution better than 200 eV. The energy range is 1 – 20 keV. The detector and electronics are identical for both SXDUs. Table 1 lists the specifications.

Table 1. Performance requirements of SXDU.

Parameter	Specification
Energy range (keV)	1–20
Energy resolution (eV)	< 200 @ 5.9 keV
Aperture area (cm <sup>2</sup> )	0.17 and 0.005
Field of view (°)	±2
Time cadence (s)	1
Count rate (counts s <sup>-1</sup> )	≥ 1 × 10 <sup>5</sup>

Figure 1 presents a conceptual sketch of the SXDUs. The SXDUs consist of X-ray Detector Modules (XDMs), analog electronic units (AEUs), a data processing unit (DPU), and a power supply unit (PSU). Collimators are positioned in front of the XDMs to restrict the field of view and aperture area. The two XDMs and their associated AEUs share a common DPU and PSU. Detector power is supplied by the low- and high-voltage power supplies within the PSU. The PSU, AEU, and DPU are interconnected via a common bus board for signal transmission and power distribution. Additionally, two temperature sensors are mounted on the AEUs to monitor temperature fluctuations on the analog board.

## III. X-RAY DETECTOR MODULE

### A. SDD detector

Silicon X-ray detectors are widely used in space applications, including silicon drift detectors (SDDs) [15–18], silicon photomultipliers [19, 20], silicon microstrips [21, 22], Si-PIN detectors [23, 24], CCD detectors [25, 26], and APS CMOS imaging sensors [27]. A 500 μm thick SDD is selected as the X-ray sensor. Its unique electrode structure provides an ultralow capacitance, enabling operation at a short peaking time, which increases the count rate. The energy resolution is further improved using a thermoelectric cooler (TEC). The SDD, along with a CMOS charge-sensitive preamplifier, is mounted on the TEC. The detector is positioned behind a thin window composed of a 150 nm silicon nitride film covered with 250 nm aluminum. The two XDMs use the same type of SDD; however, the aperture areas restricted by the collimator are 0.17 cm<sup>2</sup> and 0.005 cm<sup>2</sup>, re-

spectively. A passive graded shield surrounding the detector package protects the detector against space background radiation and fluorescent photons from surrounding materials. Additionally, two <sup>241</sup>Am radioactive sources are mounted between the detector plane and collimator in both SXDUs for in-flight calibration and self-verification.

When detector leakage current accumulates in the preamplifier, the ramp output eventually saturates. To counter this, a reset pulse is applied to restore the detector anode to ground potential, as shown in Fig. 2. The large transient caused by the reset pulse can interfere with signal processing; therefore a window of 10 μs is implemented to eliminate its effects.

### B. TEC characteristics

The detector leakage current is sensitive to the operating temperature, doubling for every 7 °C increase, as described by [28]

$$I_0 = T^2 e^{-E_g/2kT} \quad (1)$$

where  $I_0$  is the leakage current,  $T$  is the detector operating temperature,  $E_g$  is the silicon bandgap energy (which is temperature-dependent), and  $k$  is the Boltzmann constant. The TEC reduces electronic noise in the detector and preamplifier. The heat extracted by the TEC is dissipated through a mounting stud attached to a copper heat radiator. Figure 3 shows the TEC voltage and current at a room temperature of 25 °C. The SDD temperature decreases exponentially as TEC power increases, allowing the silicon detector to be cooled to –30 °C. Since the leakage current of the SDD increases after radiation exposure [29–32], the TEC temperature can be adjusted using a command. Additionally, the TEC can be turned off if necessary. The voltage and current of the TEC driver are recorded every second.

### C. Preamplifier reset rate

The preamplifier periodically resets the charge accumulated on the feedback capacitance due to X-ray signals and leakage current:

$$I_0 = C_f V_{\text{ramp}} f_{\text{reset}} \quad (2)$$

where  $I_0$  is the leakage current,  $C_f$  is the preamplifier feedback capacitance (typically 25 fF),  $V_{\text{ramp}}$  is the ramp voltage, and  $f_{\text{reset}}$  is the ramp-reset rate. The reset rate decreases exponentially with decreasing detector temperature and stabilizes at a nominal value of 12 – 13 Hz in the absence of incident radiation. However, it increases with higher incidence rates and deposited energy. To monitor variations in SDD leakage current following radiation exposure, the reset rate is recorded every second.

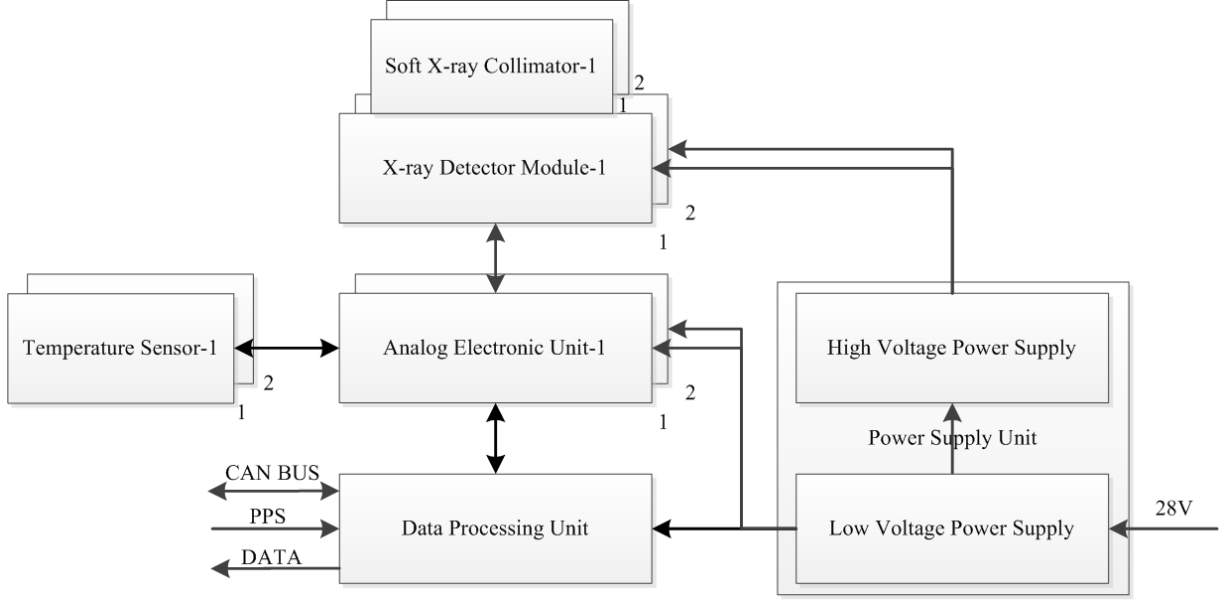


Fig. 1. SXDU functional block.

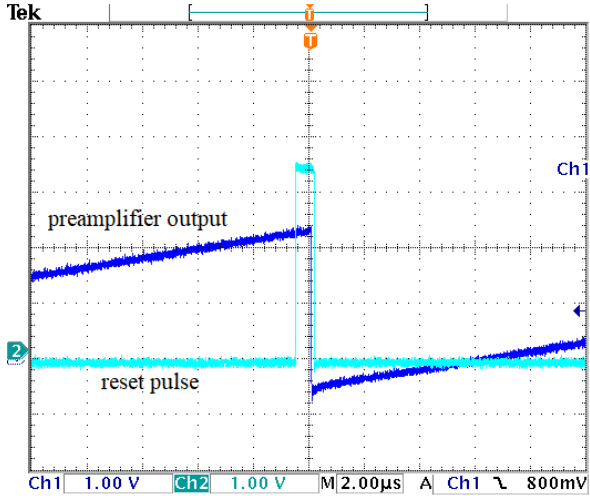


Fig. 2. (Color online) A pulse resets the ramp when saturation is reached.

#### IV. AEU

The AEU comprises an SDD preamplifier driver, TEC power driver, and front-end readout electronics, as shown in Fig. 4.

##### A. SDD and TEC drivers

The preamplifier driver circuit generates and filters power, sends reset signals to the preamplifier, and buffers and amplifies the preamplifier output to drive the front-end electronics.

The TEC driver reads the temperature diodes inside the

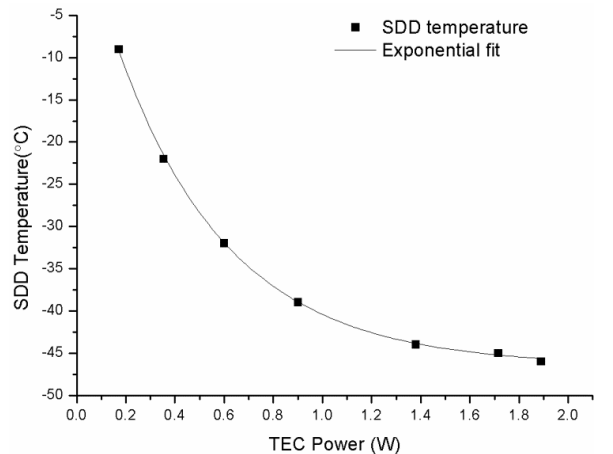


Fig. 3. Exponential temperature drop with TEC power.

SDD package and supplies power to the TEC. The temperature diode is biased using a  $160\ \mu\text{A}$  current source. A proportional-integral-derivative (PID) control feedback loop maintains the SDD at the desired temperature, which is set via a digital-to-analog converter (DAC). The TEC power is supplied by a high-efficiency DC-DC converter, with output ripple minimized using an LC-type filter. The voltage and current of the TEC driver, along with the set and measured temperatures, are converted using an ADC. These parameters, together with the ramp-reset rate, are used to assess the operational status of the SDD in orbit.

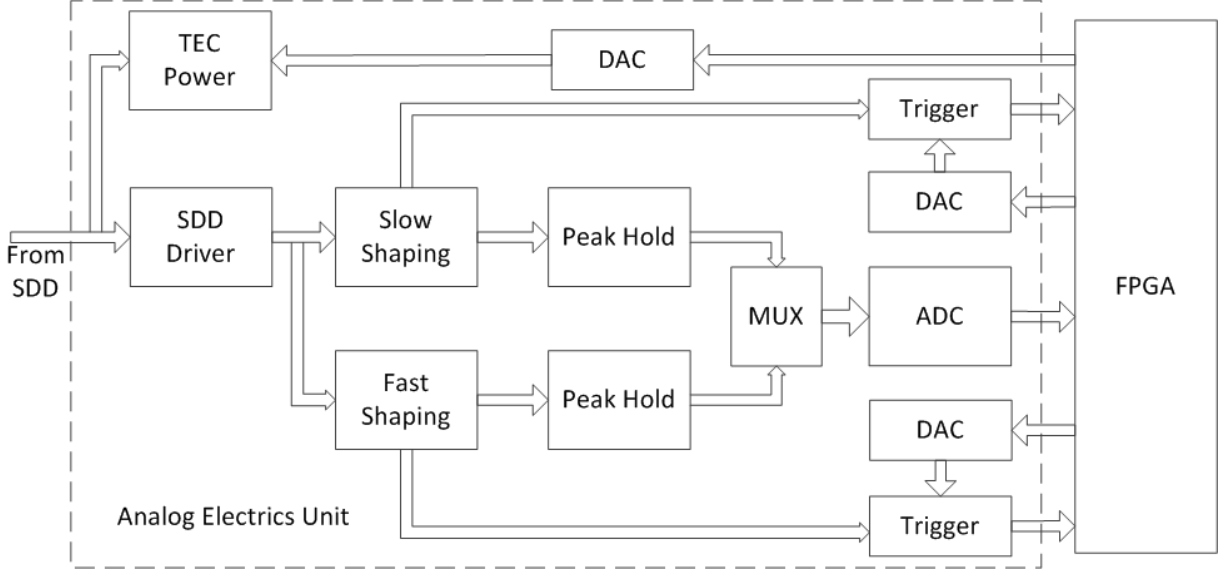


Fig. 4. AEU function blocks.

### B. Shaping amplifier

The preamplifier generates a ramp output composed of small steps. Its output is differentiated to measure the step voltage. The shaping amplifier, designed using two-pole multiple-feedback active low-pass filters [33], as shown in Fig. 5, enhances the signal-to-noise ratio. The amplifiers are optimized to achieve a Bessel phase response, ensuring a constant group delay within the passband. The step response exhibits no overshoot or ringing, which is essential for the performance of the spectrometer. While the rising edge of the shaping output is steep, the voltage decays exponentially back to the baseline. These exponential tails extend many times the duration of the full width at half maximum (FWHM). Pulses that overlap during the extended window pile-up, particularly at high count rates. Reducing the FWHM mitigates pulse pile-up but introduces additional noise.

Two parallel shaping amplifiers with different time constants are designed to serve distinct purposes. The first amplifier is optimized for better timing accuracy, while the second is designed to achieve higher spectral resolution. The shaping amplifiers, with peaking times of 315 ns and 65 ns, are referred to as “slow shaping” and “fast shaping”, respectively. The fast-shaping channel is optimized to improve double-pulse resolution and reduce pile-up; however, it introduces more noise. Consequently, a higher threshold—set by a DAC—is required. In contrast, the slow-shaping channel uses a longer peaking time to extract spectral information. When the amplitude of the slow-shaping channel exceeds the threshold, the peak value is held by the peak holder and digitized by an ADC.

Table 2 lists the design parameters of the slow-shaping channel. The group delay is simulated to be constant in the passband at 853.8 ns, as shown in Fig. 6.

A pulse generator is connected to the input of the shaping

amplifier to simulate the X-ray events. Figure 7 shows the transient response of the slow channel, revealing no overshoot and no ring. The rise time of the slow-shaping amplifier is measured to be 315 ns, the fall time is 945 ns, and the pulse width is less than 2.8  $\mu$ s.

Traditional pile-up detection is performed using a fast/slow-channel approach [34]. It cannot distinguish pulses that overlap in the fast channel. The differential of the shaping amplifier generates a bipolar output. As Fig. 8 shows, the pulse width of the differential signal is significantly smaller than that of the shaping amplifier. Therefore, the differential signals of the fast channel are selected for pile-up rejection.

The time interval of an X-ray photon can be described by an exponential distribution.

$$f(\tau) = \lambda e^{-\lambda\tau} \quad (3)$$

where  $\tau$  is the dead time and  $\lambda$  is the average incoming rate, which is assumed to be  $1 \times 10^5$  counts  $\cdot$  s $^{-1}$ . The dead time caused by the shaping amplifier is 2.8  $\mu$ s for the slow channel. The probability of a non-paralyzable pile-up can be calculated as

$$P(X \leq \tau) = \frac{\lambda\tau}{1 + \lambda\tau} \quad (4)$$

For a slow channel,  $\tau = 2.8 \mu$ s, the probability is 21.9 %. The probability is reduced to 4.8 % for a fast channel with a dead time of 0.5  $\mu$ s. The throughput is significantly better, making it suitable for calculating the true input rate.

### C. Peak-hold circuit

The rise time of the SDD output is a function of the incident position [35]. The peaking time of the slow channel is significantly longer than the variation in the rise time, with

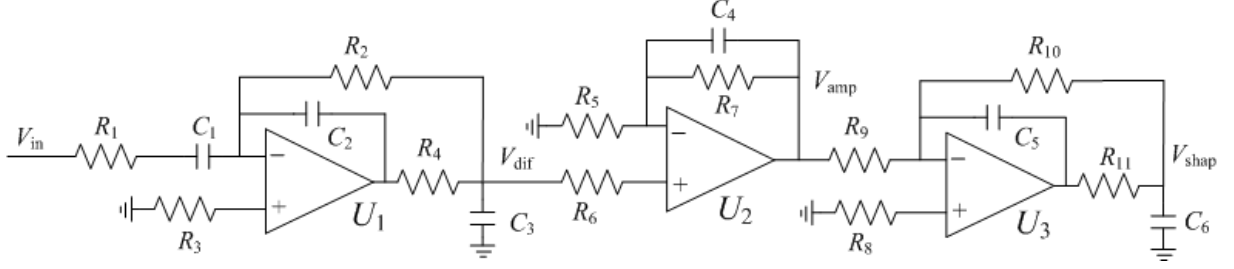


Fig. 5. Shaping amplifier circuit.

Table 2. Design parameters of the shaping amplifier.

Parameters	$R_1$ ( $\Omega$ )	$R_2 = R_3$ ( $\Omega$ )	$R_4$ ( $\Omega$ )	$C_1$ (pF)	$C_2$ (pF)	$C_3$ (pF)	$C_4$ (pF)	$R_5 = R_6$ ( $\Omega$ )	$R_7$ ( $\Omega$ )	$R_8 = R_9$ ( $\Omega$ )	$R_{10}$ ( $\Omega$ )	$R_{11}$ ( $\Omega$ )	$C_5$ (pF)	$C_6$ (pF)
Slow	200	1000	51	1200	220	1200	10	100	1500	200	1300	51	270	680
Fast	200	620	10	200	47	47	10	100	2000	200	2200	51	32	100

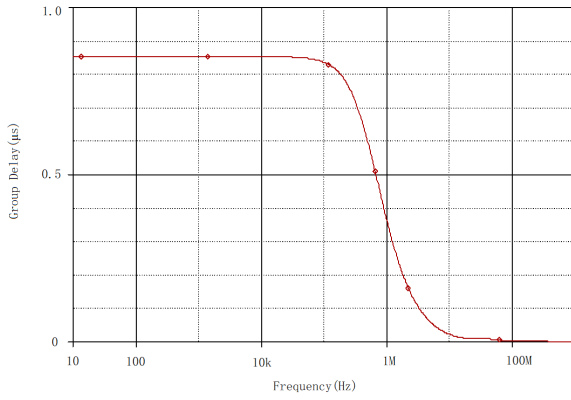


Fig. 6. Group delay simulation of the slow-shaping amplifier.

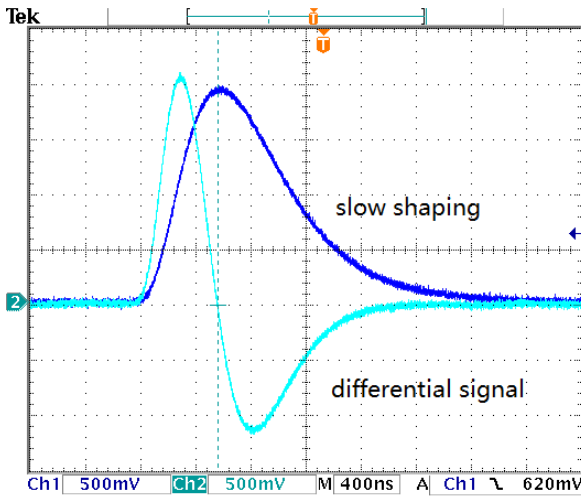


Fig. 7. (Color online) Oscilloscope traces showing the slow-shaping amplifier and differential signals.

a maximum of 30 ns. Therefore, the amplitude of the slow-channel amplitude does not depend on the event position. The flat-top duration of the fast channel is shorter than the rise

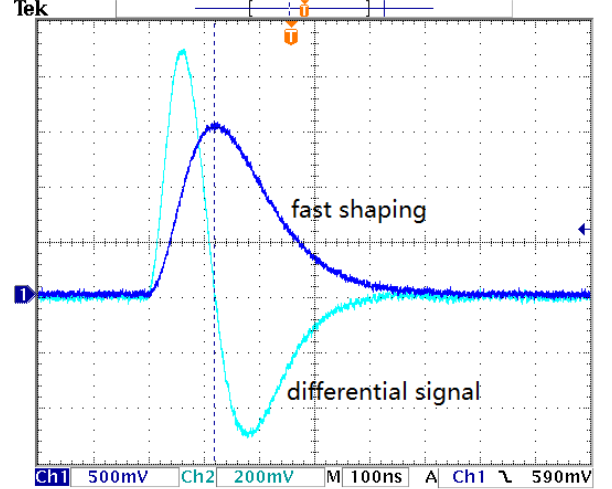


Fig. 8. (Color online) Oscilloscope traces showing the fast-shaping amplifier and differential signals.

time, leading to pulse height loss due to the ballistic deficit. As a result, events originating far from the center could be rejected by comparing the fast and slow amplitudes. Both peak values are sampled for space-background rejection.

The diagram of the peak-hold circuit is shown in Fig. 9. A CMOS analog switch is inserted between the shaping amplifier and the hold-capacitor stage. When a pulse peak is detected, the peak value is held in the capacitor by turning off the switch until it is read out by a 16-bit ADC. Only the 12 most significant bits are stored. The charge on the capacitor is reset by turning on the switch. The peak value from the capacitor is buffered by a unit-gain operational amplifier with a low input-bias current. Additionally, low-leakage, low-dielectric absorption capacitors are essential. The peak value of the fast-shaping amplitude is obtained in the same manner, with both the fast and slow peak-hold circuits sharing a common ADC. Figure 10 shows the input waveform of the ADC. A CMOS analog switch is used to select a single channel. The switch features an extremely high switching speed and

ensures break-before-make switching. The charge injection is less than 2 pC, which is crucial for high-precision peak-height capture.

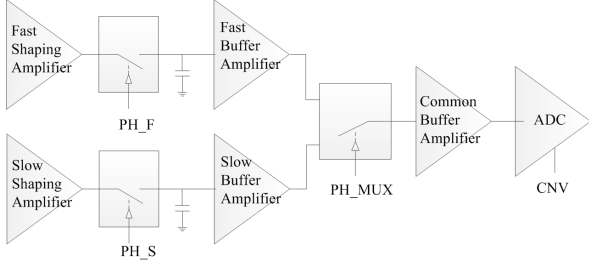


Fig. 9. Peak-hold circuit and multiplexing of two channels.

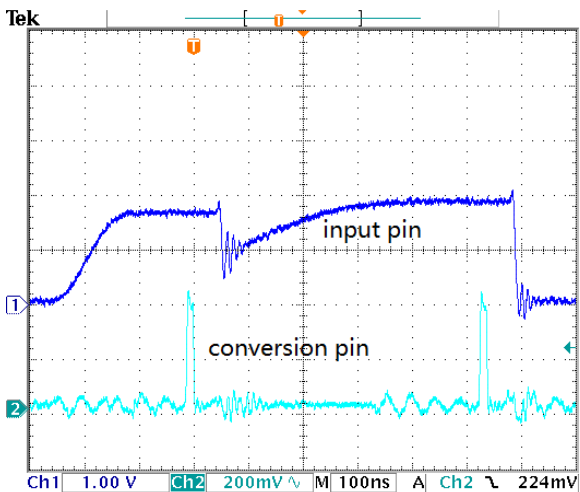


Fig. 10. (Color online) Waveform of the input and conversion pin of the peak-height ADC.

Figure 11 shows the timing of the switches in the peak-hold circuit. The durations of the peak-hold signals “PH\_F” and “PH\_S” for the fast and slow channels are 150 ns and 200 ns, respectively. The ADC starts the conversion signal, “CNV”, for the two channels with delays of 100 ns and 150 ns, respectively. At the end of each peak-hold signal, the switch changes its state. It is important to note that, in some cases, “PH\_F” may be absent, as the fast channel threshold is higher. As a result, the assertion of “PH\_MUX” is controlled by both “HOLD\_S” and “PH\_F.” Here, “HOLD\_S” is the “HOLD” signal of the slow channel, while “HOLD\_F” corresponds to that of the fast channel. At the rising edge of “HOLD\_S”, if “PH\_F” is high, then “PH\_MUX” is asserted at the falling edge of “PH\_F”; otherwise, “PH\_MUX” is asserted immediately.

The “HOLD” signal is generated by connecting the differentiating amplifier output to a comparator with hysteresis. “HOLD\_S” and “HOLD\_F” are generated in the same approach, as shown in Fig. 12 and Fig. 13. The comparator  $U_2$  output, known as “HOLD”, switches to high for input voltages greater than  $V_{HI}$  and does not switch to low until the input voltage is less than  $V_{LO}$  (i.e., at the zero crossing).

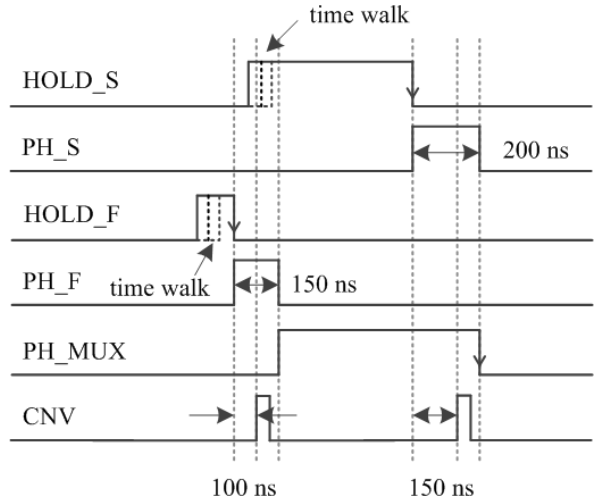


Fig. 11. Timing of the switches in the peak-hold circuit.

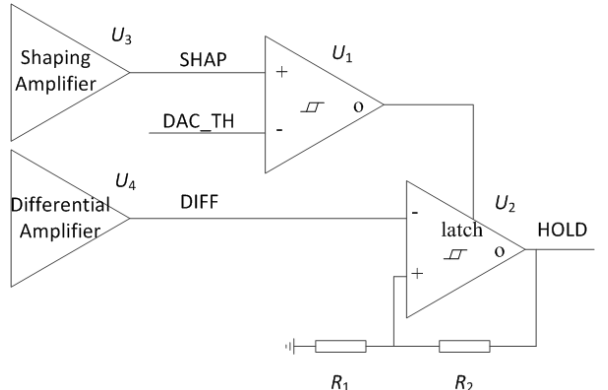


Fig. 12. Trigger logic circuit.

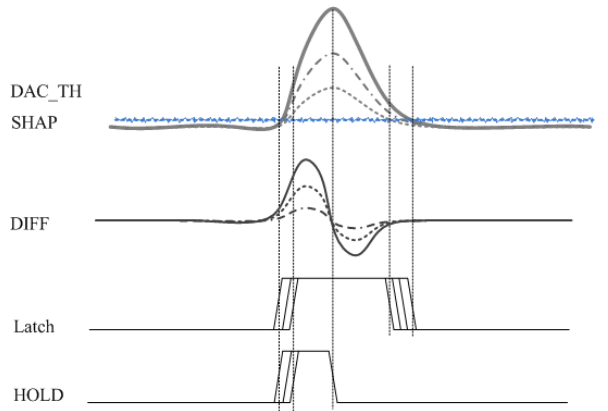


Fig. 13. Timing of trigger logic.

$$V_{HI} = (VCC - 1) \frac{R_1}{R_1 + R_2} \quad (5)$$

$$V_{Low} = 0 \quad (6)$$

where  $V_{CC} = 5\text{ V}$ ,  $R_1 = 100\Omega$ ,  $R_2 = 10\text{ k}\Omega$ , and  $V_{HI} = 40\text{ mV}$ . The latch pin of  $U_2$  is connected to the output of  $U_1$ . Therefore, the “HOLD” remains at a low state unless the shaping-amplifier amplitude exceeds the threshold.

#### D. Pile-up rejection

If the two pulses are too close in time, the height of the second pulse can be affected. Errors in the measured pulse height may distort the spectrum. The overlapping pulse in the slow channel was identified using the differential signal of the fast channel, as described earlier. To obtain a clean spectrum, all overlapping pulses are rejected. The analog shaper exhibits an infinite impulse response. Even when the tail drops rapidly toward the baseline, a small contribution remains [36]. The dead-time window widths, “WINDOW\_S” and “WINDOW\_F”, for the slow and fast channels, are  $2.8\mu\text{s}$  and  $0.5\mu\text{s}$ , respectively, as shown in Fig. 14. If an event occurs during the dead time, the dead time is reset, which reduces throughput. Therefore, the dead time can be described using a paralyzable model, as shown in Fig. 15 [37].

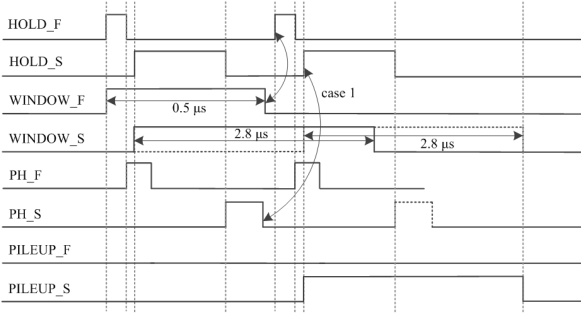


Fig. 14. Timing of pile-up rejection.

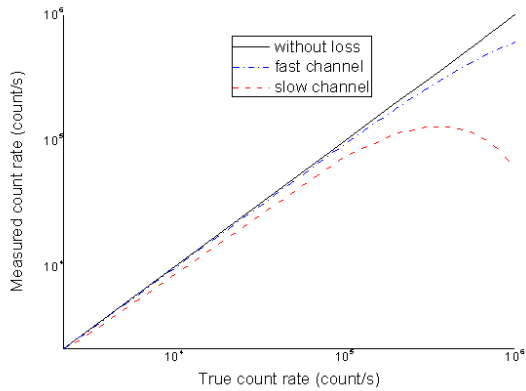


Fig. 15. (Color online) Paralyzable dead-time model.

The fraction without loss is

$$P(X > \lambda) = e^{-\lambda\tau} \quad (7)$$

In other words, the probabilities of count loss are 75.6 % and 95.1 % for the slow and fast channels, respectively. The probability of count loss is significantly higher than that of the shaping amplifier, primarily due to the dead-time window. To accurately estimate the input count rate, the “HOLD” signal of the fast channel is counted every second.

## V. OPERATING MODE DESIGN

The SXDU generates three types of observation modes, in addition to the default standby mode.

In standby mode, after being powered on, the SXDU operates with the XDMs and AEUs powered off. The selected detector channel is powered by a command. Following initialization, the SXDU switches to the selected observation mode.

The baseline noise observation mode is primarily used to enable detailed monitoring of detector performance, particularly the evaluation of noise after radiation exposure. The signal amplitude is sampled every 10 ms, regardless of the incident events.

In the spectrometer histogram observation mode, each valid pulse height is stored in its respective channel to obtain a spectrum histogram with 2048 channels. The histogram depth is 3 bytes, generating 6 KB of histogram data every second.

The photonlist observation mode samples the pulse heights in both channels sequentially using a 16-bit ADC. Data for each event consists of the detector number, trigger mode, time stamp, and pulse height data. Each transfer frame consists of 512 events, and the data capacity is limited by the interface clock to a maximum of 40 frames per second.

## VI. SPECTRAL PERFORMANCE

It is desirable to obtain a linear energy response in solar spectroscopy. Before the X-ray sources are applied, a step signal generator, instead of an X-ray detector, is connected to the front-end readout electronics. The step voltage is attenuated 80 times using a small resistor to reject noise. The sampled peak values are scaled linearly with the input voltage, as shown in Fig. 16.

A miniature X-ray tube with a W target is used to obtain the fluorescence lines from aluminum (1.49 keV), titanium (4.51 keV), manganese (5.90 keV), copper (8.05 keV), molybdenum (17.48 keV) and silver (22.17 keV). The emission line at approximately 13.94 keV from the  $^{241}\text{Am}$  radioactive source is included. Spectral performance is evaluated using the  $K_{\alpha 1}$  line centroid and width. During calibration, the detector temperature is maintained at  $-30^\circ\text{C}$ .

Figure 17 shows the linear calibration using X-ray sources. The gain and offset are obtained by linear fitting. The gain is 5.9 eV/channel when operated in the photonlist observation mode. The offset is approximately  $-233\text{ eV}$  with an error of 42 eV. The upper and lower limits of the energy range are 23.39 keV and 0.7 keV, respectively.

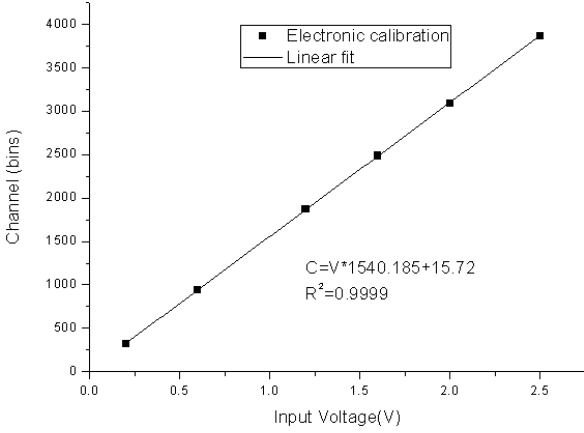


Fig. 16. Linearity response test of the front-end electronics by an electronic signal generator.

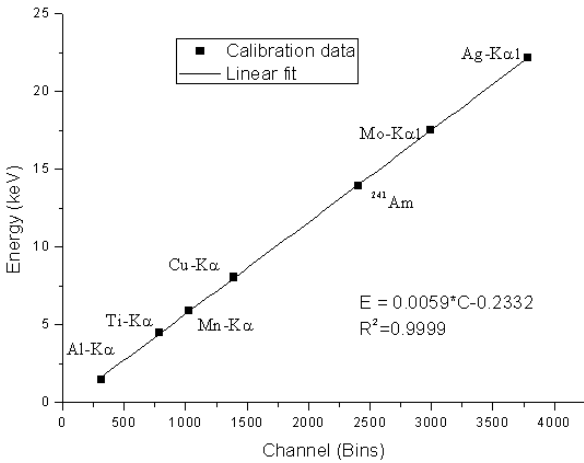


Fig. 17. Linear calibration by X-ray sources.

The energy resolution calibrated using various X-ray sources are listed in Table 3. The  $K_{\alpha}$  line is the sum of the two lines. The  $K_{\alpha 1}$  lines for  $^{241}\text{Am}$ , Mo, and Ag are shown.

Figure 18 shows the spot spectrum of the Mn fluorescence lines. The 5.90-and 6.49 keV line complexes are clearly detected. The spectral lines are fitted with a Gaussian function to obtain the peak channel centroid and FWHM. The measured energy resolution is 138 eV at 5.90 keV, which is markedly better than the requirement of 200 eV. Compared to the instruments listed in Table 4, this study demonstrates better energy resolution with a lower peaking time, indicating a higher solar flare level and better spectral resolution.

As shown in Fig. 19, the centroid drift in the temperature range of  $-5^{\circ}\text{C}$  to  $20^{\circ}\text{C}$  is less than 0.6 ADC bin, which is calibrated to approximately 3.6 eV. These results demonstrate the low noise and high accuracy of the electronic read-out design of solar X-ray spectrometers.

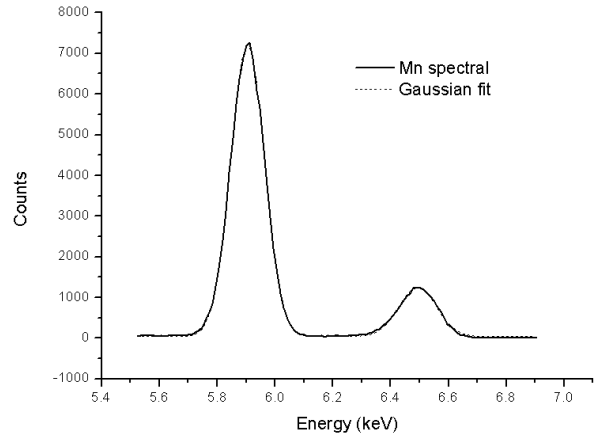


Fig. 18. X-ray detector response to Mn fluorescence illumination.

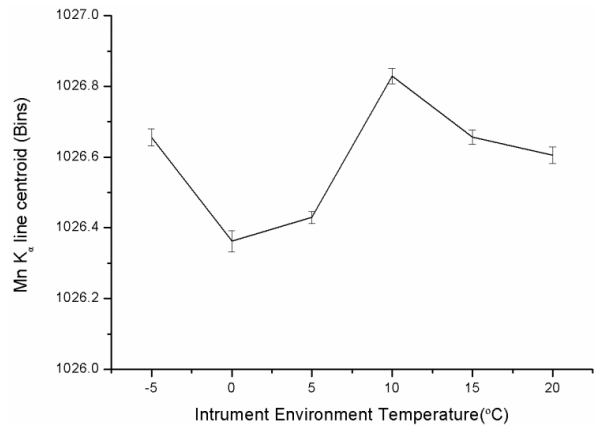


Fig. 19. Mn  $K_{\alpha}$  line centroid drifts with temperature.

## VII. CONCLUSION

This study presents the design and ground calibration of a solar soft X-ray detection unit on the MSS-1B satellite. The core component of the X-ray module is a silicon drift detector, chosen for its excellent energy resolution. The detector is nominally cooled to  $-30^{\circ}\text{C}$  using a TEC. The preamplifier output voltage is further processed by two parallel shaping amplifiers with peaking times of 315 ns and 65 ns. The slow-shaping channel, optimized for spectroscopy, operates with a higher peaking time, while the fast channel is used for pile-up rejection. The linearity response was validated using an electronic signal generator and various X-ray sources. The measured energy resolution is 138 eV at 5.90 keV, with a centroid drift of less than 3.5 eV over a temperature range of  $-5^{\circ}\text{C}$  to  $20^{\circ}\text{C}$ . Compared with other on-orbit solar X-ray instruments, this study demonstrates improved energy resolution with a lower peaking time, enabling higher sensitivity to solar flare levels and better spectral resolution. These results highlight the low-noise, high-accuracy read-out electronics design of the solar X-ray spectrometer.

Table 3. The energy resolution calibrated by various X-ray sources.

X-ray Source	Energy (keV)	FWHM(eV)	Error(eV)
Al-K <sub>α</sub>	1.49	96.97	1.10
Ti-K <sub>α</sub>	4.51	127.16	0.44
Mn-K <sub>α</sub>	5.90	138.00	0.42
Cu-K <sub>α</sub>	8.05	165.68	1.98
<sup>241</sup> Am	13.94	221.62	4.05
Mo-K <sub>α1</sub>	17.478	238.45	20.85
Ag-K <sub>α1</sub>	22.162	262.28	17.78

Table 4. The energy resolutions of solar X-ray detectors.

Instrument	SXRS [6]	HEPP-X [7]	SXM [13]	MinXSS [8]	This study
Sensor	SDD	SDD	SDD	SDD	SDD
Sensor area	7 mm <sup>2</sup>	7 mm <sup>2</sup>	30 mm <sup>2</sup>	25 mm <sup>2</sup>	25 mm <sup>2</sup>
Energy range	1.5 – 24.8 keV	0.9 – 35 keV	1 – 15 keV	0.5 – 30 keV	0.7 – 23.97 keV
Field of view	±26°	±30° × ±50°	±40°	±2°	±2°
Energy resolution	185 eV @ 5.88 keV	175 eV @ 5.90 keV	175 eV @ 5.90 keV	168 eV @ 5.90 keV	138 eV @ 5.90 keV
Peaking time	/	/	1.0 μs	1.2 μs	315 ns
Count rate	/	10 kcps	80 kcps	255 kcps	100 kcps
Cadence	2.05 s	/	1 s	10 s	1 s

- [1] S.F. Wang, Y.N. Zhang, W. Cui, X-ray tomography of hidden matter in the Universe. *Sci. Bull.* **86**, 3120–3123 (2023). DOI: [10.1016/j.scib.2023.11.033](https://doi.org/10.1016/j.scib.2023.11.033)
- [2] K.K. Zhang, A novel geomagnetic satellite constellation: science and applications. *Earth Planet Phys.* **7**, 4–21 (2023). DOI: [10.26464/epp2023019](https://doi.org/10.26464/epp2023019)
- [3] A. Reinard, S. Hill, S. Bailey et al., Report on GOES SX-I/XRS calibration effort. In: Fineschi S, Viereck R A, eds. *Proceedings of Solar Physics and Space Weather Instrumentation II*, San Diego, California, USA, **6689**, 66890J (2007) DOI: [10.1117/12.734268](https://doi.org/10.1117/12.734268)
- [4] P.C. Chamberlin, T.N. Woods, F.G. Eparvier et al., Next generation X-ray sensor (XRS) for GOES-R Satellite Series. In: Fineschi S, Fennelly J A, eds. *Proceedings of Solar Physics and Space Weather Instrumentation III*, San Diego, California, USA, **7438**, 743802 (2009). DOI: [10.1117/12.826807](https://doi.org/10.1117/12.826807)
- [5] B.R. Dennis, K.J.H. Phillips, R.A. Schwartz et al., Solar flare element abundances from the Solar Assembly for X-Rays (SAX) on MESSENGER. *ApJ.* **803**, 67 (2015). DOI: [10.1088/0004-637X/803/2/67](https://doi.org/10.1088/0004-637X/803/2/67)
- [6] F. Wei, X.X. Zhang, B.Q. Zhang et al., Pre-flight calibration and the first results for the solar X ray spectrometer (SXRS) onboard FY-2F satellite. *Chin. J. Geophys. (in Chinese).* **57**, 3812–3821 (2014). DOI: [10.6038/cjg20141135](https://doi.org/10.6038/cjg20141135)
- [7] X.Q. Li, Y.B. Xu, Z.H. An et al., The high-energy particle package onboard CSES. *Radiat. Detect. Technol. Methods.* **3**, 1–11 (2019). DOI: [10.1007/s41605-019-0101-7](https://doi.org/10.1007/s41605-019-0101-7)
- [8] C.S. Moore, A. Caspi, T.N. Woods et al., The instruments and capabilities of the miniature X-ray solar spectrometer (MinXSS) cubeSats. *Sol. Phys.* **293**, 21 (2018). DOI: [10.1007/s11207-018-1243-3](https://doi.org/10.1007/s11207-018-1243-3)
- [9] J.P. Mason, T.N. Woods, P.C. Chamberlin et al., MinXSS-2 cubesat mission overview: improvements from the successful MinXSS-1 mission. *Adv. Space Res.* **66**, 3–9 (2020). DOI: [10.1016/j.asr.2019.02.011](https://doi.org/10.1016/j.asr.2019.02.011)
- [10] B.D. Schwab, R.H.A. Sewell, T.N. Woods et al., Soft X-ray observations of quiescent solar active regions using the novel dual-zone aperture X-ray solar spectrometer. *ApJ.* **904**, 20 (2020). DOI: [10.3847/1538-4357/abba2a](https://doi.org/10.3847/1538-4357/abba2a)
- [11] T.N. Woods, B. Schwab, R. Sewell et al., First results for solar soft X-ray irradiance measurements from the third generation miniature X-ray solar spectrometer. *ApJ* **956**, 94 (2023). DOI: [10.3847/1538-4357/acef13](https://doi.org/10.3847/1538-4357/acef13)
- [12] H.E. Spence, A. Caspi, H. Bahcivan et al., Achievements and lessons learned from successful small satellite missions for space weather-oriented research. *Space Weather.* **20**, e2021SW003031 (2022). DOI: [10.1029/2021SW003031](https://doi.org/10.1029/2021SW003031)
- [13] N.P.S. Mithun, S.V. Vadawale, A. Sarkar et al., Solar X-ray monitor on board the Chandrayaan-2 orbiter: in-flight performance and science prospects. *Sol. Phys.* **295**, 139 (2020). DOI: [10.1007/s11207-020-01712-1](https://doi.org/10.1007/s11207-020-01712-1)
- [14] Y.Q. Shi, L.S. Li, J.W. Chen et al., Design of the solar X-ray detector for the macau science satellite-1B. *Earth Planet Phys.* **7**, 125–130 (2023). DOI: [10.26464/epp2023018](https://doi.org/10.26464/epp2023018)
- [15] F. Zhang, H.Y. Wang, W.X. Peng et al., High resolution solar soft X-ray spectrometer. *Chin. Phys. C.* **36**, 146–150 (2012). DOI: [10.1088/1674-1137/36/2/008](https://doi.org/10.1088/1674-1137/36/2/008)
- [16] F. Wei, S.J. Wang, J.B. Liang et al., Next generation Space Environment Monitor (SEM) for FY-2 satellite series.(in Chinese). *Chin. J. Geophys.* **56**, 1–11 (2013) DOI: [10.6038/cjg20130101](https://doi.org/10.6038/cjg20130101)
- [17] X.H. Fu, C.L. Li, G.L. Zhang et al., Data processing for the Active Particle-induced X-ray Spectrometer and initial scientific results from Chang'e-3 mission. *Res. Astron. Astrophys.* **14**, 1595 (2014) DOI: [10.1088/1674-4527/14/12/008](https://doi.org/10.1088/1674-4527/14/12/008)
- [18] E.L. Chen, C.Q. Feng, S.B. Liu et al., Readout electronics for a high resolution soft X-ray spectrometer based on silicon drift detector. *Nucl. Sci. Tech.* **28**, 14 (2016). DOI: [10.1007/s41365-016-0160-0](https://doi.org/10.1007/s41365-016-0160-0)
- [19] J.X. Wen, X.T. Zheng, J.D. Yu, et al., Compact CubeSat Gamma-ray detector for GRID mission. *Nucl. Sci. Tech.* **32**, 99 (2021). DOI: [10.1007/s41365-021-00937-4](https://doi.org/10.1007/s41365-021-00937-4)
- [20] Y.P. Liu, P. Dang, X.B. Tang et al., Performance analysis of LYSO-SiPM detection module for X-ray communication during spacecraft reentry blackout. *Nucl. Instrum. Meth. A* **1013**, 165673 (2021). DOI: [10.1016/j.nima.2021.165673](https://doi.org/10.1016/j.nima.2021.165673)
- [21] J.J. Wei, J.H. Guo, Y.M. Hu et al., Characterization of silicon microstrip sensors for space astronomy. *Nucl. Sci. Tech.* **31**, 97 (2020). DOI: [10.1007/s41365-020-00811-9](https://doi.org/10.1007/s41365-020-00811-9)

- [22] Y.X. Cui, X. Li, S. Wang et al., Simulation of DAMPE silicon microstrip detectors in the Allpix2 framework. *Nucl. Instrum. Meth. A* **1057**, 1168685 (2023). [DOI: 10.1016/j.nima.2023.168685](#)
- [23] Y. Tan, X.L. Cao, W.C. Jiang et al., In-orbit performance of ME onboard Insight-HXMT in the first 5 years. *Radiat. Detect. Technol. Methods* **7**, 15–24 (2023). [DOI: 10.1007/s41605-023-00395-z](#)
- [24] Y.G. Ye, H. Zou, Y.F. Wang et al., A cross-type imaging electron spectrometer. *Sci. China Tech. Sci.* **66**, 641–653 (2023). [DOI: 10.1007/s11431-022-2103-7](#)
- [25] Y.H. Guo, S.W. Peng, F. Wei et al., Design and simulation of Soft X-Ray imager on SMILE satellite (in Chinese). *Chin. J. Geophys.* **61**, 4348–4355 (2018). [DOI: 10.6038/cjg2018L0734](#)
- [26] Y. Chen, W.W. Cui, W. Li et al., The Low Energy X-ray telescope (LE) onboard the Insight-HXMT astronomy satellite. *Sci. China Phys. Mech. Astron.* **63**, 249505 (2020). [DOI: 10.1007/s11433-019-1469-5](#)
- [27] C.Zhang, Z.X. Ling, X.J. Sun et al., First Wide Field-of-view X-Ray Observations by a Lobster-eye Focusing Telescope in Orbit. *Astrophys. J. Lett.* **941**, L2 (2022). [DOI: 10.3847/2041-8213/aca32f](#)
- [28] H. Spieler, Semiconductor detector systems. (Oxford, Oxford University Press, 2005), pp. 1–42.
- [29] B.Q. Zhang, F. Wei, S. Leng et al., Effect on characteristic of silicon drift detector by electron exposure (in Chinese). *J. Beijing Univ. Aeronaut. Astronaut.* **39**, 235–238, (2013).
- [30] E.D. Monte, Y. Evangelista, E. Bozzo et al., The effect of the displacement damage on the charge collection efficiency in silicon drift detectors for the LOFT satellite. *J. Instrum.* **10**, P05002 (2015). [DOI: 10.1088/1748-0221/10/05/P05002](#)
- [31] M. Shanmugam, Y.B. Acharya, S.V. Vadawale et al., Radiation effects on Silicon Drift Detector based X-ray spectrometer onboard Chandrayaan-2 mission. *J. Instrum.* **10**, P09005 (2015). [DOI: 10.1088/1748-0221/10/09/P09005](#)
- [32] M. Shanmugam, S.V. Vadawale, A. Patel et al., Investigation of radiation damage due to particle irradiation on Silicon Drift Detector for Chandrayaan-2 mission. *J. Instrum.* **15**, P01002 (2020). [DOI: 10.1088/1748-0221/15/01/P01002](#)
- [33] G. Prigozhin, K. Gendreau, J.P. Doty et al., NICER instrument detector subsystem: description and performance. In: Herder J A., Takahashi T, Bautz M, eds. *Proceedings of Space Telescopes and Instrumentation 2016: Ultraviolet to Gamma Ray*, Edinburgh, United Kingdom, **9905**, 99051I (2016). [DOI: 10.1117/12.2231718](#)
- [34] G. Blaj, C.J. Kenney, A. Dragone et al., Optimal pulse processing, pile-up decomposition, and applications of silicon drift detectors at LCLS. *IEEE Trans. Nucl. Sci.* **64**, 2854–2868 (2017). [DOI: 10.1109/TNS.2017.2762281](#)
- [35] G. Prigozhin, K. Gendreau, R. Foster et al., Characterization of the silicon drift detector for NICER instrument. In: Holland A D, Beletic J W, eds. *Proceedings of High Energy, Optical, and Infrared Detectors for Astronomy V*, Amsterdam, Netherlands, **8435**, 845318 (2012). [DOI: 10.1117/12.926667](#)
- [36] R.H. Redus, A.C. Huber, D.J. Sperry, Dead time correction in the DP5 digital pulse processor. In: *IEEE Nuclear Science Symposium Conference Record*, Dresden, Germany, 3416–3420 (2008). [DOI: 10.1109/NSSMIC.2008.4775075](#)
- [37] S. Usman, A. Patil, Radiation detector deadtime and pile up: A review of the status of science. *Nucl. Eng. Technol.* **50**, 1006–1016 (2008). [DOI: 10.1016/j.net.2018.06.014](#)